Ring faulting and piston collapse in the mantle sustained the largest submarine eruption ever documented

E. Jacques, Roser Hoste-Colomer, N. Feuillet, A. Lemoine, J. van der Woerd, W.C. Crawford, C. Berthod, P. Bachèlery

Earth Planet. Sci. Lett. 647 (2024) 119026

Contents lists available at ScienceDirect

Earth and Planetary Science Letters

journal homepage: www.elsevier.com/locate/epsl

Ring faulting and piston collapse in the mantle sustained the largest submarine eruption ever documented

E. Jacques [a,*], R. Hoste-Colomer [b], N. Feuillet [a], A. Lemoine [b], J. van der Woerd [c], W.C. Crawford [a], C. Berthod [d], P. Bachèlery [e]

[a] Université Paris Cité, Institut de Physique du Globe de Paris, Equipe de Géosciences Marines, CNRS, Paris, France
[b] BRGM, French Geological Survey, Direction Risks and Prevention, Orléans, France
[c] Institut Terre et environnement de Strasbourg, UMR 7063, CNRS, Université de Strasbourg, ENGEES, Strasbourg, France
[d] Observatoire volcanologique et sismologique de Guadeloupe, Institut de Physique du Globe de Paris, Gourbeyre, France
[e] Université Clermont Auvergne, CNRS, IRD, OPGC, Laboratoire Magmas et Volcans, Clermont-Ferrand, France

ARTICLE INFO

Keywords:
Mayotte
Basaltic submarine eruption
Mantle earthquakes
Volcano-tectonic seismicity
New piston collapse model
Magmatic plumbing system

ABSTRACT

The basaltic submarine eruption offshore the island of Mayotte between July 2018 and January 2021 is one of the largest documented underwater eruptions. One of the most striking differences between this eruption and most documented eruptions is the exceptional depth of the associated seismicity, which is limited almost exclusively to the lithospheric mantle. This seismicity probably outlines magma reservoirs and dyking zones.

In order to better understand the deep processes driving the eruption, we analyze precise earthquake locations and focal mechanisms associated with this event. We present a set of 2677 accurate earthquake relocations and 300 focal mechanisms determined from data collected over the first 9 months of ocean bottom seismometer deployments, starting in February 2019.

Our relocations refine the structure of two swarms (Proximal and Distal with respect to Mayotte), and reveal well-defined mantle structures between 20 and 55 km below sea level, which we interpret as a ring-fault zone and a dyke, respectively. The Proximal swarm outlines a ring-fault zone as the locus of a large piston collapse caused by the deflation of an underlying magma reservoir. Deformation around the piston is driven by normal faulting on a set of inward dipping patches surrounding the piston. Locally, collapse of the conical shaped piston causes a radial extensional stress field with strike-slip and normal faulting ruptures accommodating the relaxation of the damaged zone around the piston.

This piston collapse allowed the transfer of lava to the eruption site via the dyke highlighted by the Distal earthquake swarm. The link between the swarms is thus magmatic, in agreement with petrological analyses of lava from the new volcano.

This is the first time that piston collapse and localized dyking have been documented in the mantle. The pattern of deformation documented here could apply to shallower, crustal piston collapses, such as in Iceland.

1. Introduction

The Comoros archipelago lies between the eastern coast of Africa and Madagascar (Fig. 1) and is composed of four main islands: Grande Comore, Moheli, Anjouan and Mayotte. A large submarine eruption started east of Mayotte Island, likely between late June and early July 2018 (Lemoine et al., 2020; Mercury et al., 2022), and it ended between December 2020 and January 2021 (REVOSIMA, 2024; Berthod et al., 2022; Lavayssière et al., 2024). The eruption gave birth to Fani Maoré, a 5 km diameter, 820 m high volcano at the tip of a NW-SE striking volcanic ridge ~50 km east of Mayotte (Feuillet et al., 2021) likely emplaced along preexisting and/or newly formed tectonic structures between the Somali and Lanwdle plates (Famin et al., 2020; Feuillet et al., 2021; Thinon et al., 2022). A total of 6.5 km^3 of lava poured out onto the seafloor. The eruption was associated with exceptionally deep seismicity seated between 20 and 55 km in the mantle part (Feuillet et al., 2021) of an old Mesozoic oceanic lithosphere (Masquelet et al., 2024). Swarms of deep M4–5 earthquakes as intense as those in Mayotte

* Corresponding author.
E-mail address: jacques@ipgp.fr (E. Jacques).

https://doi.org/10.1016/j.epsl.2024.119026
Received 19 June 2024; Received in revised form 4 September 2024; Accepted 22 September 2024
Available online 11 October 2024

have never been observed, not even during the 2011–2013 El Hierro submarine eruption (Canary archipelago, e.g. Martí et al., 2013) or the 2021 eruption of La Palma, (e.g. Torres-González et al., 2020; D'Auria et al., 2022).

After the most intense phase of the magmatic event that occurred from December 2018 to February 2019, about 30,000 earthquakes were recorded between the end of February 2019 and mid-May 2020 in two separate swarms located 5–15 km and 25–45 km distant from Petite-Terre Island, east of Mayotte (Fig. 1a): the Proximal and Distal swarms (REVOSIMA, 2024). The largest earthquake was a magnitude 5.9 event. About fifty events were M5+ and hundreds were felt by the population (Mercury et al., 2022; Saurel et al., 2022). The distribution of the seismicity along with other data (GNSS models, tomography, petrology, geology, bathymetry) was used to propose various models for what led to this extraordinary eruption (Fig. 1). However, the locations of earthquakes were too imprecise to image clearly the geological structures involved, preventing a clear understanding of the eruptive processes. Moreover as these structures are exceptionally deep in the mantle (20–55 km), we lack analogs worldwide. Although, earthquakes in the mantle are more common in the oceanic domain (e.g. Kuna et al., 2019; Grevemeyer et al., 2019; Craig et al., 2014), than in continental tectonic domains (e.g. Lavayssière et al., 2019; Déverchère et al., 2001; Blanchette et al., 2018; Inbal et al., 2016; Monsalve et al., 2006), they are still too rare and too sparse to reveal clear lithospheric-scale structures. Imaging of large intraplate faults across the entire oceanic lithosphere by seismic reflectors (Singh et al., 2017) however suggest that faults can break the whole lithosphere to cause large M7–8+ earthquakes. Here we document for the first time very well localized lithosphere scale volcano-tectonic structures activated during a major magmatic event. The period covered by our study extends from late February 2019 to mid-November 2019. It begins just after the phase during which the highest magma fluxes feeding the eruption were inferred (> 400 m^3/s, between December 2018 and February 2019, Peltier et al., 2022). In November 2019, the inferred magma fluxes were lower but still significant (between 60 and 100 m^3/s, Peltier et al., 2022) and the eruption was still vigorous. We have thus analyzed a period during which magmatic processes and related deformation could be well documented. We exploited a dense dataset from onshore and ocean bottom seismometers (OBS) and performed HypoDD relocations, with precisions higher by an order of magnitude compared to previous 1D locations. We calculated 300 focal mechanisms to characterize their kinematics and we investigated the interaction between the mantle brittle failures and the plumbing system to propose a new scenario for the Mayotte submarine eruption, which is the largest ever documented.

The Eruption

The magmatic activity started on May 10 2018, with a M5-class earthquakes swarm. During the first two months the seismicity was recorded by a very sparse seismic network. As a result, only M_L 3+

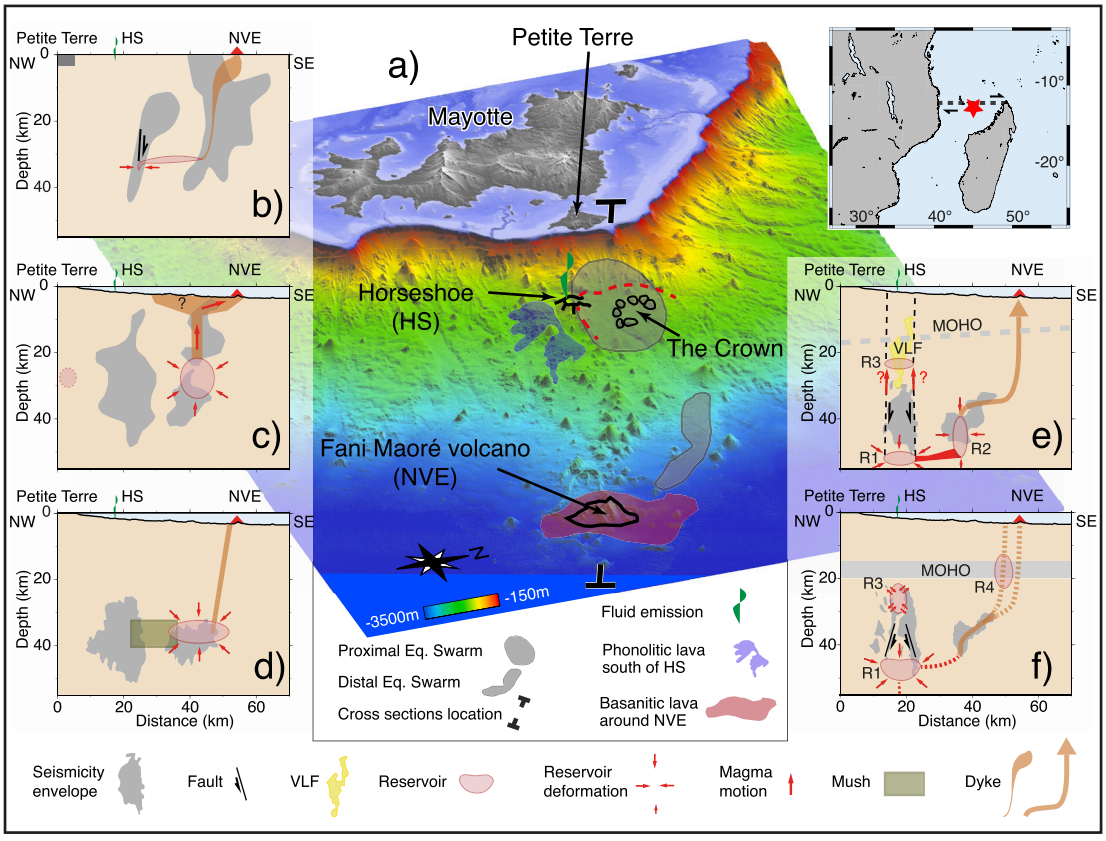

Fig. 1. (a) Three-dimensional (3D) perspective view of Mayotte Island and its eastern slope (threefold vertical exaggeration). Fani Maoré: new volcanic edifice (NVE) and its basanitic lava flows are shown by black contour and reddish shape, respectively. Red dotted line: caldera fault (inferred by Feuillet et al., 2021); Horseshoe and the Crown are volcanic vents and structures related to the inferred caldera fault. The two light-gray shapes are projections on the sea-floor of the envelopes of the Proximal and Distal earthquake swarms that we relocated between February and November 2019 and that are related to the Fani Maoré eruption.
Top right inset: geographic setting, red star: location of Fani Maoré eruption and black dotted line: nascent transform plate boundary between Somali and Lwandle plates (e.g. Feuillet et al., 2021). (b -f) Previous models of the Fani Maoré eruption, with their inferred volcano-tectonic structures and available seismicity, are shown along a vertical N113°E striking cross-section. Location of cross-section is indicated by two opposites T on (a). Explanations of the models are given in the text and detailed in Sections 1 of the supplementary text. (b) Model of Cesca et al. (2020). (c) Model of Lemoine et al. (2020). (d) Model of Mittal et al. (2022). (e) Model of Feuillet et al. (2021). (f) Model of Lavayssière et al. (2022).

events (Lemoine et al., 2020; Mercury et al., 2022), among which 37 M_L+5 with magnitude up to 5.9, were detected (Mercury et al., 2022). Later, between February 2019 and May 2020, thanks to recurrent deployments of OBS carried out during the MAYOBS cruises (Rinnert et al., 2019), five thousands earthquakes, including ten M_L5+ events with magnitude up to 5.5 were located (Saurel et al., 2022). This seismicity occured off Mayotte in the Proximal and Distal swarm locations (Fig. 1a). From mid-July 2018, the magmatic event was associated to exceptional surface deformations up to 20 cm/yr recorded by six GNSS stations located on Mayotte Island (Peltier et al., 2022). Elastic models of these deformations suggested the drainage of a 30–40 km deep reservoir located 30 km from the eastern shore of Mayotte. The distribution of the seismicity along with other information provided by various data (GNSS models, petrology, seafloor morphology) was used to propose several models for the eruption. Cesca et al. (2020) proposed the propagation of a dyke and the collapse of a caldera (Fig. 1b). However, by using data from both world-wide seismological stations and one local accelerometer in Mayotte, the earthquakes were too few and their locations too imprecise to image the structures involved. Their model proposed that the volcanic processes occurred in the crust and the magma path was mainly deduced from the position of Fani Maoré (Data from Mayobs 1 cruise, Feuillet, 2019). From onshore seismometers data and GNSS

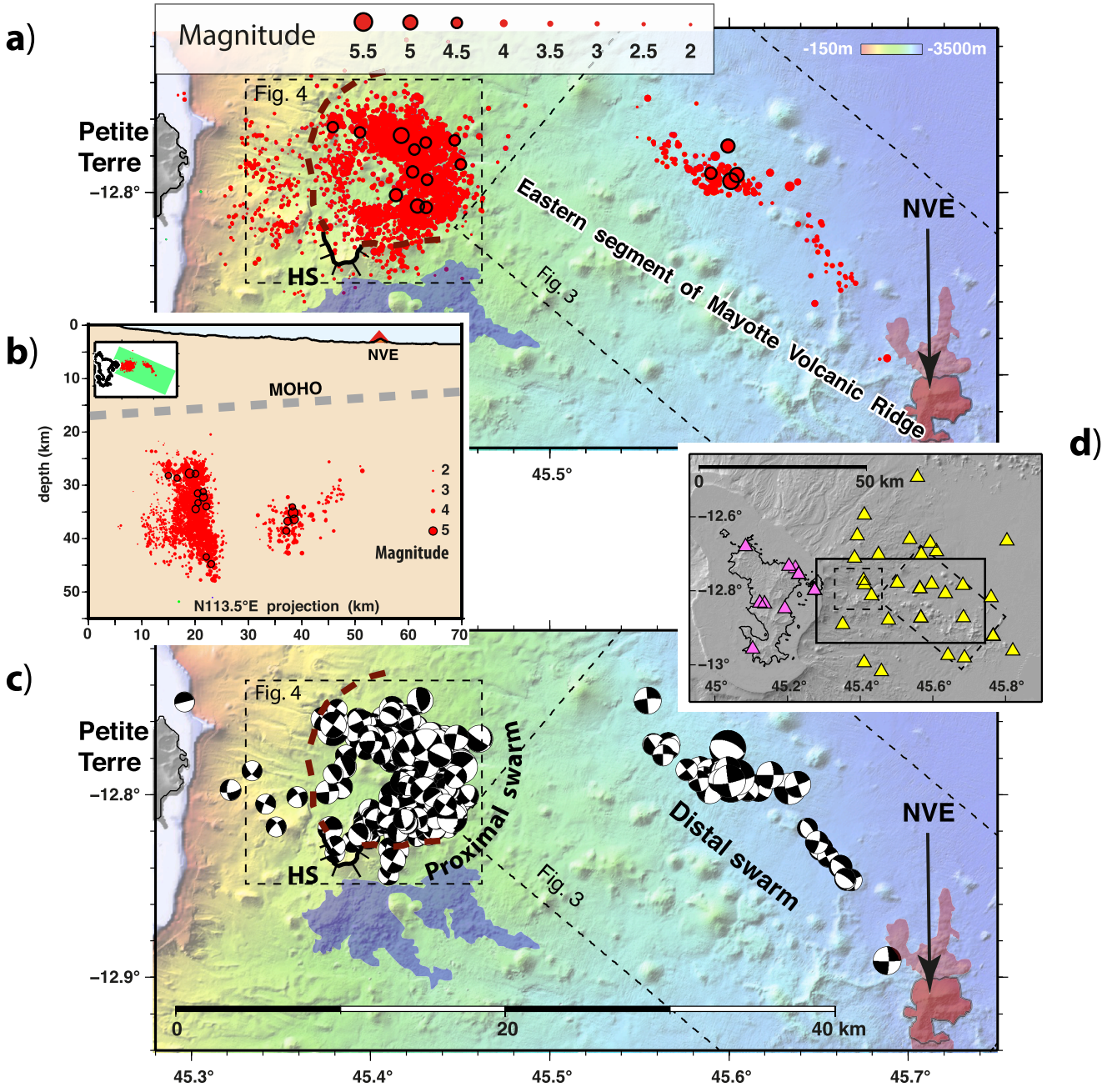

Fig. 2. Seismicity between 25 February and 19 November 2019 accompanying the Fani Maoré eruption. (a) Map of HypoDD relocations (this study) of the 2677 best events of the catalog of Lavayssière et al. (2022) in red. Dashed black boxes show locations of Figs. 3a and 4a.
(b) N113.5°E depth cross-section. No vertical exaggeration for seismicity projection. Small map inside: location of projection box (in green). Topographic profile located in the middle of projection box. The Moho profile is based on 2 Moho depth estimates. Below the Mayotte Island, receiver function analysis (Dofal et al., 2021) suggest a Moho depth around 17 km bsl. Under the new Fani Maoré volcano (NVE), according to the results of a recent seismic refraction experiment the Moho is at 14 km bsl (Masquelet et al., 2024). (c) Focal mechanisms of 300 $\sim 3 \leq M_L \leq 5.1$ earthquakes (this study) using our relocations. (d) Map of the seismological network used for the earthquake relocations. Pink and yellow triangles: land and ocean bottom stations, respectively. Thin black box shows location of Fig. 2a,c.

models, Lemoine et al. (2020) inferred the drainage of a 30 km deep reservoir, the propagation of a dyke toward the seabed and a second smaller source of deflation poorly located (Fig. 1c). From OBS data and better earthquake locations, Feuillet et al. (2021) proposed a lithosphere scale dyking and the collapse of a caldera structure in the mantle (Fig. 1e). They inferred at least three reservoirs: R1 at 55 km below the interpreted caldera structure, R3 at the at the base of the crust below seafloor structures named the Crown and the Horseshoe and R2 below the eastern Mayotte Ridge at 40 km depth, but could not image precisely the subsurface caldera structure. They inferred that the magma path sourced from R1 and intercepted R2 before reaching the surface, which is consistent with the petrological results of Berthod et al. (2021a). Mittal et al. (2022), based on GNSS inversions and on the earthquake catalog of Saurel et al., 2022, proposed the drainage of a reservoir fed by magma flux from an adjacent permeable mush zone (Fig. 1d) could explain the exceptional eruption duration without other process such as collapse of the roof reservoir. However, they don't clarify what drives the Proximal swarm. Lavayssière et al. (2022) outlined the dyke and R3 with better located earthquakes (Fig. 1f), thanks to a velocity model they inverted for. R3 was previously imaged by Foix et al. (2021) as an area of high Vp, low Vs and high Vp/Vs beneath the Crown and Horseshoe; they interpreted it as a subcrustal reservoir with mush (melt and cristal), in light of the results of Berthod et al. (2021b), who propose the existence of phonolitic magma stored close to the Moho that fed for example the phonolitic lavas south of the Horseshoe volcano (Fig. 1a). Sections 1 and 2 of the supplementary text provide more details on the cited models and more information regarding R1–4, respectively.

There is still no consensus on what led to this remarkable eruption. How those magmatic reservoirs interacted with the fault system of the caldera structure to maintain this exceptional eruption is unknown mainly because the plumbing system and the seismogenic structures are likely exceptionally deep in the mantle, the seismic monitoring network was sparse at the beginning of the event, the GNSS network geometry is unfavorable to precisely characterize the related source(s) of deformation and again we are missing analogs worldwide.

2. Methodology and data

We relocated 2677 earthquakes and calculated 300 focal mechanisms (Figs 2a-c). We used the seismological data collected during six cruises (MAYOBS 1, 2, 3–4, 6, 7 and 8, Rinnert et al., 2019) on bord of RV Marion Dufresne and recorded between 25/02/2019 and 19/11/2019. The different deployments included at least 5 and up to 17 operating OBS's from INSU and Ifremer (two French institutes: National Institute for Earth Sciences and Astronomy & National Institute for Ocean Science), which complemented the land stations (up to 9) of the local network (Fig. 2d, Saurel et al., 2022).

2.1. Relative relocation of manually picked earthquakes by using Hypo DD

We performed a relative relocation of earthquakes with the double-difference method using HypoDD 2.1 software (taking into account station elevations relative to sea level, Waldhauser, 2001). We selected the 2680 best-located events from the catalog of Lavayssière et al. (2022) that were located using the NonLinLoc location software (Lomax et al., 2014). We relocated these events (Fig. 2a) using 39,574 P- and 34, 171 S-phases with the same 1D, local velocity model (for the P and S waves) that Lavayssière et al. (2022) inverted using VELEST (Kissling et al., 1995). Two earthquakes form a pair of events if: 1) their hypocenters are within 200 km of the recording seismic stations; 2) they are separated by <20 km; 3) they have at least 8 links (number of pair phases). We employed the conjugate gradients method LSQR (Paige and Saunders, 1982) to solve double-difference equations, and for each layer we used a Vp/Vs ratio, which varies as determined by Lavayssière et al. (2022). With those criteria and methods, we could relocate 2677 events, considered as the best characterized earthquakes. Location uncertainties for each epicenter range between 100 and 400 m for >98% of the events (**supp Fig. 1.1**). The depth is also well constrained with uncertainties <300 m for 94% of the events and probably <200 m for events whose depth ranges between 30 and 42 km (**supp Fig. 1.1**). Section 3 of the supplementary text file gives more details regarding the assessment of location uncertainties.

2.2. Focal mechanisms inversion

We determined 300 double couple (DC) focal mechanisms using P-wave polarities (Fig. 2c) that were manually picked during collaborative « pickathons » (Saurel et al., 2022). We only considered the earthquakes with local magnitude (M_L) greater than or equal to ~3. We used FPFIT v1.5 (July 13, 2011, Reasenberg et al., 1986) for the focal mechanism inversion. The input locations were our HypoDD relocations previously described. The azimuth and takeoff angles were computed with Hypo71 (Lee and Lahr, 1972) by forcing the locations to stay at our HypoDD relocations and using the same local P wave velocity model.

We only used picks from stations within 500 km of the epicenters (**supp Fig. 2**). Beyond this distance, the assumption of a flat-layered earth is unrealistic (we used a 1D velocity model for our relocations) and polarities are rarely available. The five farthest stations are a station on Grande Glorieuse Island (225–245 km), three stations from the Karthala network of Grande Comore (235–280 km) and the northern-most station of Madagascar (475–500 km).

The 300 focal mechanisms, which include seventeen M4.5+ events, were determined with at least 12 polarities (except one M4.5+ earthquake with 11 polarities). On average, there are 15 P wave polarities per focal mechanism. Azimuthal gap values range from 44° to 123°, except for two events of the Distal swarm, whose values are 150° and 209° (see details in Section 5 of the supplementary text).

Moment tensors can be decomposed into double-couple (DC), isotropic (ISO), and compensated linear vector dipole (CLVD) components (e.g. Tkalčić et al., 2009). Volcanic systems are particularly prone to non-DC mechanisms. As FPFIT is not adapted to detect non-DC focal mechanisms, for each focal mechanism we determined, we verified, that the distribution of the first P polarities on the focal sphere cannot be explained by mechanisms having predominant ISO or CLVD components.

3. Results

3.1. Distribution of the seismicity

Our relocated seismicity highlights very fine and localized structures in the mantle (Fig. 2, **supp Video 1**). Most of the events (2513) are in the Proximal swarm while the Distal swarm only contains 164 events (Fig. 2a). The depths of events range between 25 and 43 km below sea level (bsl) in the Distal swarm, and between 20 and 55 km bsl in the proximal swarm (Fig. 2b). There is no obvious evolution of the distribution, neither in depth nor in map view over the analyzed time period **(supp Fig. 3).**

From W to E, the Distal swarm stretches over a distance of 25 km in a 5 km-wide band, trending N110°E to 150°E (Fig. 3). It is made of two sub-clusters: a northwestern sub-cluster trending N110–120°E and a southeastern subcluster trending ~N130°E. The northwestern subcluster consists of 127 events lying between 32 and 43 km bsl and gathering in a subvertical, ~8 km long, ~10 km high and ~4 km wide zone (Fig. 3a-c), whereas the southeastern subcluster consists of 37 events forming a 1 km-thin, 65° NE dipping zone that shallows towards Fani Maore volcano (Fig. 3a, d and **supp 3D Videos 1 and 3**). It is noteworthy that most of the southeastern subcluster events occurred towards the end of our catalog, between early August and 19 November 2019 (**supp Fig. 3**).

In map view, the Proximal swarm looks like a 13 km wide donut with

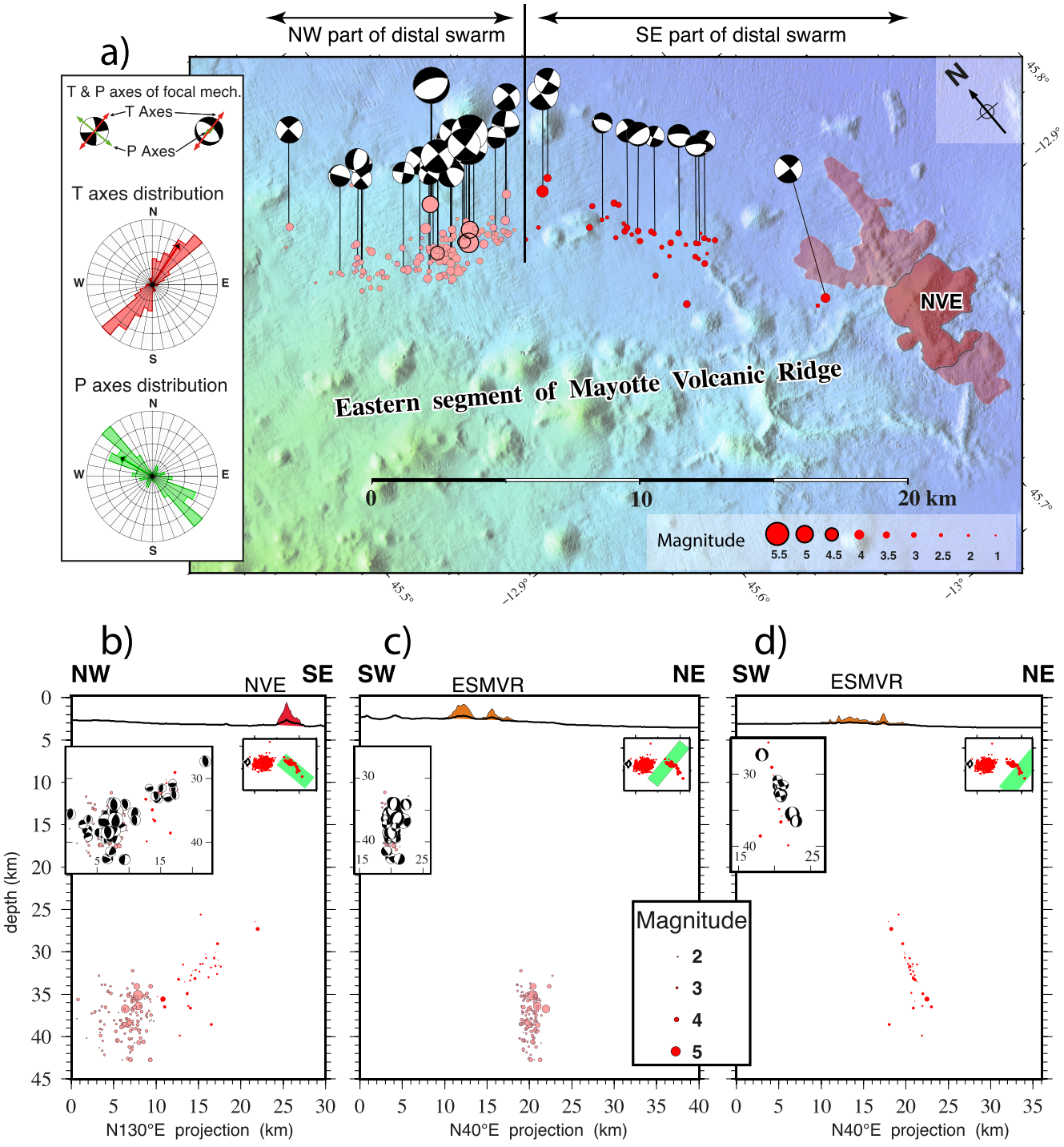

Fig. 3. Distal swarm 25 February – 19 November 2019. (a) Seismicity map, with related focal mechanisms. Light-red and red circles: NW and SE parts of Distal swarm. Color Scale of sea-floor depth as in Fig. 2a. Inset: Rose diagrams of horizontal projections of T and P axes of focal mechanisms, in red and green colors, respectively. (b) N130°E depth cross-section of whole Distal swarm. (c) N40°E depth cross-section of NW part of Distal swarm. (d) N40°E depth cross-section of SE part of Distal swarm. Orange shapes along topographic profiles show the Eastern segment of Mayotte Volcanic Ridge (ESMVR), the Fani Maoré volcano (NVE) is shown in red. No vertical exaggeration for seismicity projections. Topographic profiles are located in the middle of the projection boxes. Right insets: green boxes used for earthquake selection for each of the 3 projections. Left insets: Focal mechanisms drawn on the corresponding cross-sections.

a 3–4 km wide hole (Fig. 4). Eighty-four percent of the Proximal swarm events (99% of the released seismic moment) are concentrated in the southern, eastern and northern quarters of the donut, whereas the seismicity is much more diffuse in the western quarter.

Four 2 km-wide vertical cross-sections (Fig. 4c-f) with different azimuths and intersecting at the center of the Proximal swarm show that the earthquakes are mainly distributed between 25 and 50 km bsl. Between 30 km and 45 km bsl, they gather to form 2–4 km thin, outward-dipping 70–90° linear structures that are very well defined.

In 3D, these structures form a 15 km-high truncated-cone whose diameter is 8 km at the base and 4 km at the top and whose lateral flank is about 2–3 km thick (4 km at most), see also the 3D video (**supp Video 2**). Most M4.5+ earthquakes we relocated occurred in the eastern part of the conical structure (Fig. 4a, d-f).

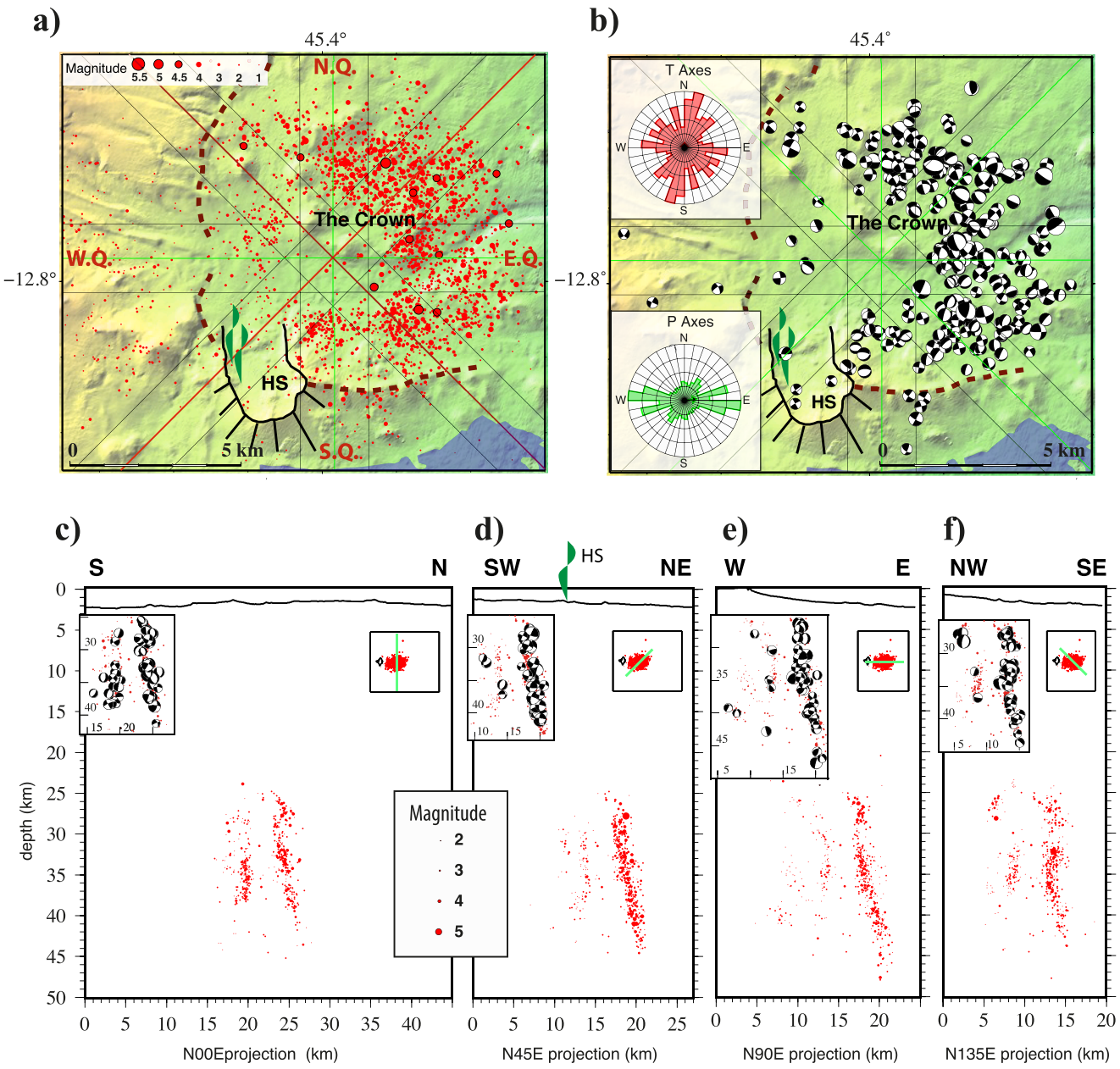

Fig. 4. Proximal swarm 25 February – 19 November 2019. (a) Seismicity map, same color scale of sea-floor depth as in Fig. 2a. Red lines delimit 4 quarters (N.Q., E.Q., S.Q and W.Q.) of Proximal swarm. Green wavy symbol: location of fluid emissions in Horseshoe crater (HS). (b) Focal mechanisms map. Green lines with associated 2-km wide bands that are delineated by thin black lines, are cross-sections in c, d, e and f. Upper and lower insets in b: rose diagrams of horizontal projections of focal mechanisms T (red) and P (green) axes, respectively. (c-f) Depth cross-sections of seismicity, along N00°E (c), N45°E (d), N90°E (e) and N135°E (f) directions. No vertical exaggeration for seismicity projections. Green wavy symbol as in (a). Right insets show green boxes used for earthquake selection of each of the 4 projections boxes. Left insets: Focal mechanisms drawn on the corresponding cross-sections.

Above, between 25 and 30 km, the seismicity is more diffuse and appears to underline an ovoid shape that is particularly clear in Fig. 4f. This ovoid's major axis is ~7 km long in the NW-SE direction. No earthquake was relocated inside.

3.2. Focal mechanisms

The focal mechanisms are presented in Figs. 2b, 3, and 4 and in the Supplementary information (supp **Table 1 and supp Fig. 4**). The 40 focal mechanisms of the Distal swarm are exclusively strike-slip and normal faulting events (Fig. 3a). Their T axes strike between N00°E and N60°E, with most of them striking NE-SW.

The 260 focal mechanisms we determined in the Proximal swarm are more varied. Most of them are strike-slip and normal faulting events, but about ten are thrust events (Fig. 4b). The orientations of T axes of the mechanisms show a quasi-radial distribution with a slight distribution peak in the N10°$E \pm 10°$ azimuth (**inset** of Fig. 4b). About 80% of T axes strike ±45° toward the center of the conical structure (Fig. 5a**, supp Fig. 5b**). Between 30 km and 45 km bsl, within the flank of the conical structure they are plunging 20–30° inward on average. Above, around the ovoid structure from 25 km to 30 km bsl their plunge ranges from 0° to 20 to 30° inward; outside the structures they are generally sub-horizontal (Fig. 5c-d). The orientations of P axes are less scattered and show a peak of distribution in the N90±20° azimuth. The distribution peaks of the P and T axis orientations are rotated by 30–40° counter-clockwise with respect to those of the Distal swarm.

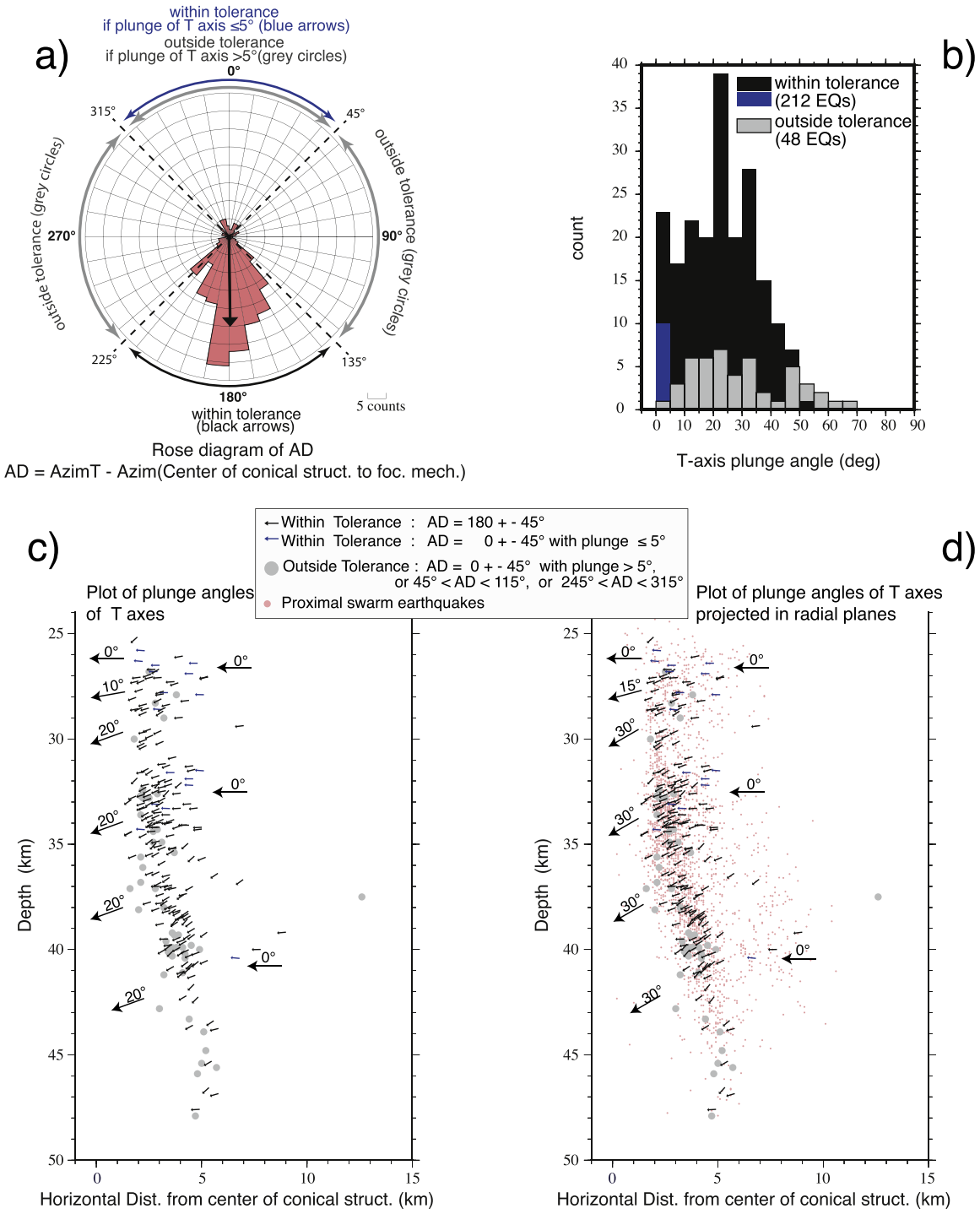

Fig. 5. T axes orientations analysis of Proximal swarm focal mechanisms.
(a) Rose diagram of angular differences (AD) between azimuth of T axes (T) and azimuth of conical structure center to position of focal mechanism. Distribution AD maximum at 180±10°, 78% of AD are within 135–225°, indicating that most T axis strike toward center of structure and plunge inward. We distinguish focal mechanisms within tolerance (80%): those with AD = 180 ± 45° and those with AD = 0 ± 45° with plunge angle ≤ 5° (sub-horizontal T, by taking into account uncertainties in focal plane parameters (supp. Table 1b)). (b) Histograms of T plunge angles. (c) T plunges (small arrows) as a function of depth and distance to vertical axis of conical structure. Plunge for outside tolerance mechanisms not shown. Large arrows indicate average plunge with depth inside and outside conical or ovoid structures. (d) Same as (c) but with T projected in the radial planes.

In cross-section, we observe that the steepest nodal planes of the normal faulting mechanisms, located along the eastern flank of the truncated cone dip by 70 to 90° toward its interior (Fig. 4c-f). These likely represent the ruptured fault plane, as normal faults generally dip steeper than 45° As the dips of these normal fault planes remain fairly constant with depth, they organize in an en-echelon array. The same observation can be made along the western flanks of the cone although the normal faulting mechanisms are sparser.

4. Discussion

All the earthquakes we relocated and their focal mechanisms are

evidence for brittle failure on well-localized structures in the upper part of the mantle. Below 30 km bsl, the Proximal swarm reveals a steep dipping, ~15 km high truncated-cone structure (Fig. 4c-f and **supp 3D videos 1 and 2**). This structure resembles those highlighted by earthquakes during caldera collapse above a draining volcanic reservoir, as for example at Mount Pinatubo (Philippines, e.g. Mori et al., 1996), Rabaul volcano (Papua New Guinea, e.g. Jones and Stewart, 1997) and Axial Volcano (Juan de Fuca Ridge, e.g. Baillard et al., 2019); except that the structure offshore Mayotte is in the mantle instead of the crust.

Analog models for caldera collapse indicate that the subsidence is driven by outward-dipping ring faults (reverse faults) that propagate upward to reach the surface (e.g. Roche et al., 2000; Acocella, 2007). However, the shallowest earthquakes we relocated are 20 km beneath the seafloor and only ten of the focal mechanisms are reverse. Instead, we determined 79 predominantly normal focal mechanisms, indicating dip-slip motion on steep 70–90° inward-dipping fault planes organized in en-echelon arrays in a narrow ~3 km wide zone along the outward-dipping conical structure (Fig. 4c-f, Fig. 6a). Similar shear patterns have been observed on natural outcrops in the field and in analog experiments in strike-slip tectonic contexts as a result of horizontal shear accompanied by volume increase (Fig. 6b, e.g. Vialon, 1979; Gamond, 1983; Nicolas, 1984). The normal fault patches we documented could be analogs of the P-type secondary shears that we interpret to accommodate subsidence of the inner part of the cone (Fig. 6a). Moreover, within the conical structure, the inward plunges of most of the T axes of the focal mechanisms (Fig. 5c-d) are consistent with the stress field that would be expected to accompany such a shear along the structure. The quasi-absence of seismicity inside the conical structure suggests that this volume moved like a rigid block: a piston. As this piston is conical, a gap should open between the piston and its surrounding wall during its downward motion. In a brittle lithosphere this should be counterbalanced by elastic radial expansion/relaxation in a damage zone around the piston (Figs. 6a,c), which is probably what promoted the strike-slip faulting with a quasi-radial distribution of T axes.

Subsidence of rigid blocks (pistons) resulting in caldera collapse has been inferred to occur during large basaltic intrusions in Iceland, Hawaii, Japan, Vanuatu, La Réunion (e.g. Gudmundsson et al., 2016;

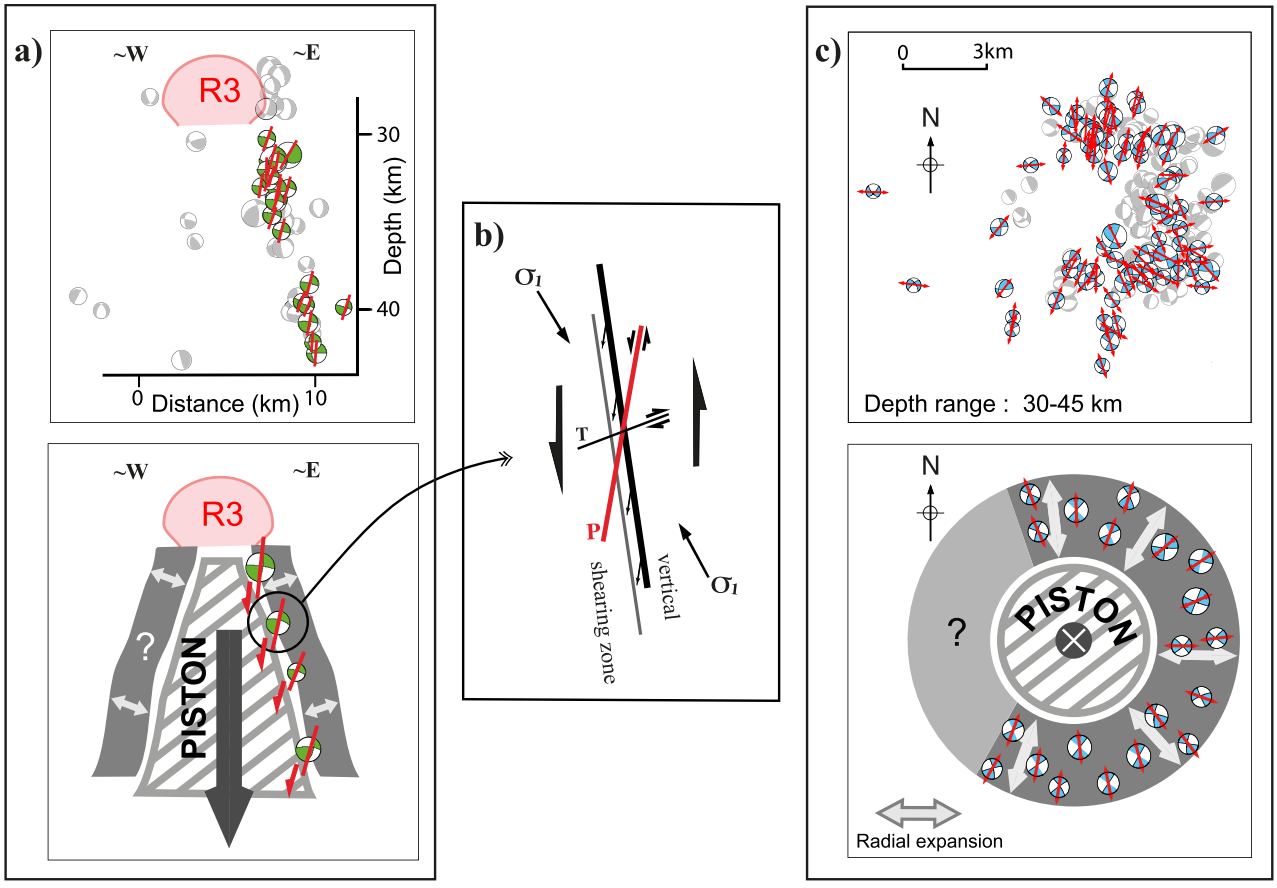

Fig. 6. Interpretation of brittle processes at work in Proximal swarm related to piston-like structure.
(a) Shearing zone around piston caused by its fall. Upper figure: W-E cross-section across the piston and expanding zone. Green and white beach balls: predominantly normal focal mechanisms, small red lines: inward-dipping, normal fault planes. Other mechanisms are in light grey and white. Lower figure: interpretative vertical cross-section across the piston, ring-fault zone and its damage zone. Grey hatch pattern: falling piston. White zone around piston: space that tends to open. Grey area around piston: its expanding/relaxing wall caused by piston fall. White double arrows: radial extension of the wall. Reddish elliptical shape: R3 reservoir. Green and white beach balls: normal focal-mechanisms with the ruptured fault plane (small red lines), note that inward-dipping, ruptured fault planes tend to concentrate close to inner rim of expanding zone and form en echelon arrays along the piston. The shear process along the piston appears identical to that described in map view in (b) but transposed vertically.
(b) Map view representation of secondary P and T shears associated to horizontal shearing along a vertical strike-slip fault plane (thick black line), with volume increase in the shear zone (shown by a grey line and small thin black arrows) during analog experiments, redrawn from Nicolas (1984).
(c) Wall expansion/relaxation around piston caused by its fall. Upper figure: map of calculated focal mechanisms around the piston between 30 and 45 km depths. Blue and white beach balls are focal mechanisms predominantly strike-slip, double thin red arrows are their T axes. Other mechanisms are in light grey and white. Lower figure: interpretative horizontal cross-section across the piston, ring fault zone and its damaged zone, with same color code and pattern as in (a). Blue and white beach balls: strike-slip focal-mechanisms with their T axes (double red arrows) radially distributed around the piston and plunging inward.

Neal et al., 2019; Shreve et al., 2019; Toda et al., 2002; Staudacher et al., 2009; Sigmundsson, 2019). Piston collapse helps to sustain the pressure in the plumbing system and maintain eruptions tens kilometers distant from the feeding reservoir (e.g. Bonny et al., 2018).

The piston within Mayotte's Proximal swarm is as large as the one involved in the 2014–2015 Bardarbunga eruption (10 km across and up to 12 km high, Gudmundsson et al., 2016). Strikingly, steep (60–90°) inward dipping normal faulting events along the northern and southern rim of the Bardarbunga caldera were also inferred from ~200 faulting mechanisms (Ágústsdóttir et al., 2019; Rodríguez-Cardozo et al., 2021), which suggested an array of faults rather than a single ring fault. This agrees with our results, although they obtained a significantly smaller proportion of strike-slip events and no evidence for a radial pattern of the T-axis distribution.

We propose that at Mayotte a piston collapse occurred at depths below 30 km-bsl, along inward, normal, en-echelon distributed faulting for which we know of no analog. This piston subsided above a deep, sub-lithospheric reservoir (R1, Feuillet et al., 2021) that was located below 45 km bsl (Fig. 7). Above the piston, we interpret that the ovoid shape highlighted by the shallowest earthquakes (25–30 km) corresponds to a subcrustal R3 reservoir inferred by Feuillet et al. (2021) from the localization of very low frequency events, by Foix et al. (2021) from the seismic wave velocity anomalies they evidenced and from the petrological results of Berthod et al. (2021b) and by Lavayssière et al. (2022) from well-located seismicity.

The N130°E striking, 13 × 10 km^2 wide, 65° NE dipping and 1 km-thin planar ascending zone of hypocenters we imaged in the Distal swarm likely represents a dyke along which the magma was transported from R1 towards the Fani Maoré volcano. This was also suggested by previous studies (Feuillet et al., 2021; Lavayssière et al., 2022) but we show the mechanisms and pathways much more precisely. The ascending "SE subcluster" group of hypocenters, which is the shallower part of the Distal swarm, is clearly connected to the deeper, more compact "NW subcluster" of the Distal swarm. Earthquakes in the NW subcluster could be promoted by pressure changes in the third reservoir (R2) inferred by Feuillet et al. (2021) below the eastern part of the Mayotte ridge (Fig. 1e). Lemoine et al. (2020) and Feuillet et al. (2021) interpreted that the compact deeper part of the Distal seismic swarm was the first activated at the onset on the magmatic unrest and the longer-lasting one. This is also near where the GNNS models determined a deflating pressure source (Lemoine et al., 2020; Feuillet et al., 2021; Peltier et al., 2022).

Along the ascending "SE subcluster" of the Distal swarm, the focal mechanisms imply ruptures along steep ~E-W right-lateral or N-S left-lateral strike slip faults and on NW-SE striking normal faults. Strike-slip faulting has been documented in other areas during dyke intrusions associated with eruptions (e.g. 2000 Miyakejima eruption in Japan, Toda et al., 2002) or with rifting episodes (e.g. the 2014–2015 Bardarbunga rifting episode in Iceland, Ágústsdóttir et al., 2016, 2019). The strike-slip and normal mechanisms along the inferred dyke are consistent with the CMT solutions of the largest M5+ earthquakes that occurred during the initial phases of the Mayotte crisis between May and June 2018 and previously (Bertil et al., 2021). The orientations of their P and T axes are compatible with NE-SW trending extension. This is in agreement with the regional stress field deduced from the geometry and kinematics of volcanic structures in the Comoros archipelago (Feuillet

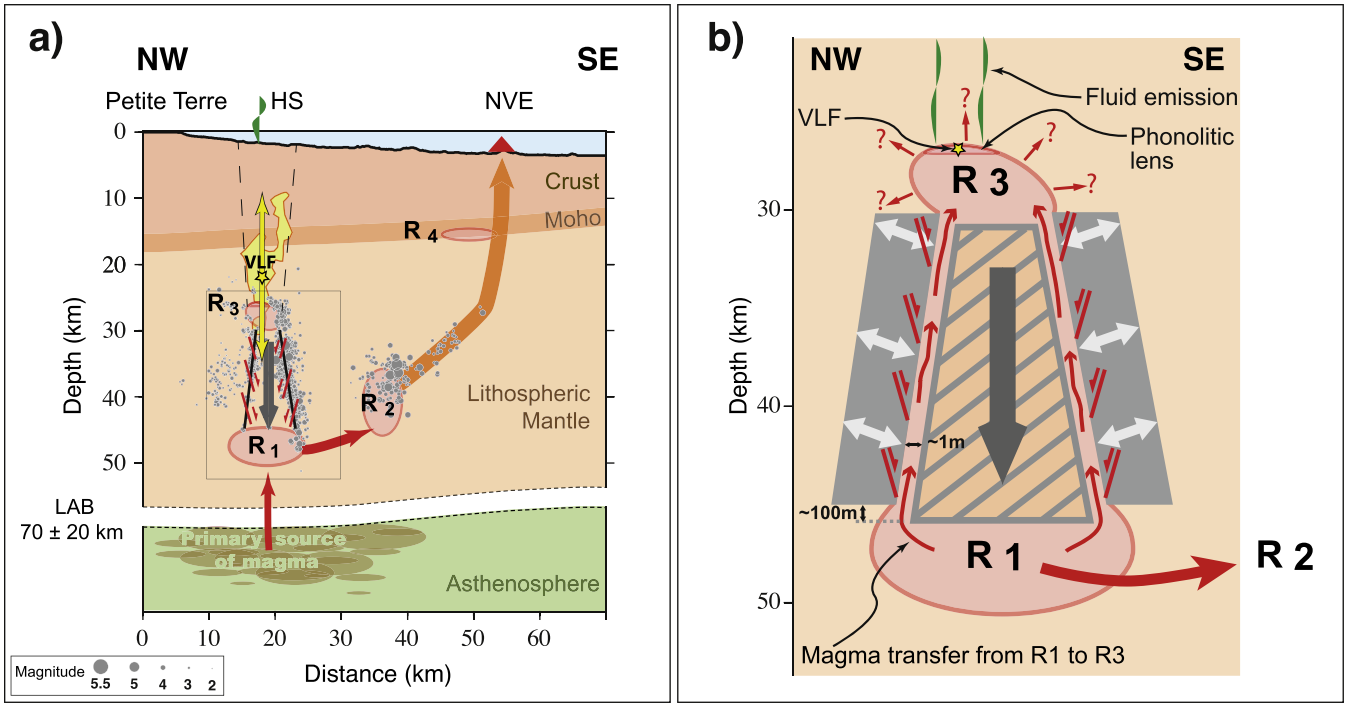

Fig. 7. (a) Schematic cross section showing the magma transfer between the Proximal swarm and the Distal swarm related to the dyke feeding the eruption and to the piston fall caused by the draining of the basal reservoir R1 (no vertical exaggeration). Elliptical reddish shapes: R1-R4 magma reservoirs. Curved, thick red arrow: aseismic magma feeding. Large orange arrow: dyke feeding the Fani Maore Volcano (NVE). Grey circles: February-November 2019 seismicity (accurate relocations using OBS data, this study). Black lines: outward dipping ring-fault system around the falling piston. Small red lines and arrows: inward dipping ruptured normal fault patches. Thick grey arrow: piston fall. Yellow shape: very low frequency earthquakes (VLF), yellow star and double arrows: mean VLF location and its uncertainty (Laurent, 2023; Laurent et al., 2019). Green wavy symbols: fluid emission. Thin black dashed lines: inferred shallower caldera structures modified from Feuillet et al. (2021). LAB: Lithosphere Astenosphere Boundary (Mazzullo et al., 2017; Barruol et al., 2019). Thin black box shows location of (b).
(b) Interpretative close-up of the ring fault system and magma transfer related to the piston fall. This figure is not strictly at scale, in order to show the space open (~1 m) around piston by its fall of ~100 m according to our model. Grey hatch pattern: falling piston. Two grey areas: wall and damage zone around piston. White double arrows: radial extension caused by piston fall. Red lines: inward-dipping, normal ruptured fault patches. Red curved or undulated, arrows around piston: magma transfer from R1 to R3. Green wavy symbols as in (a). Note the small phonolitic lens on top of R3.

et al., 2021; Thinon et al., 2022) and from regional GNSS data (Lemoine et al., 2020). The inferred dyke parallels the N130°E Eastern Mayotte ridge (Fig. 1) and may be part of a long-term volcano-tectonic system that has constructed this ridge.

It is noteworthy that most of the earthquakes highlighting the inferred dyke occurred along a narrow zone, suggesting that there was only one restricted pathway for the magma between R2 and the seafloor between February and November 2019. Furthermore, most of these earthquakes occurred from early August to mid-November 2019 suggesting an increase of magma flux in the dyke during this period. Their occurrence coincided with a new phase of magmatic activity northwest of Fani Maoré (the "third phase" of Berthod et al., 2022).

The mechanical behavior of the structures in the Proximal swarm is very different, with a quasi-radial distribution of the inward plunging T axes of its focal mechanisms (Fig. 4) indicating a local perturbation of the regional stress field. Fig. 4b shows, however, a slight dominance of N10°E striking T axes, suggesting a N10°E extension in this area. This suggests a slight counterclockwise rotation of the regional stress along the upper slope of Mayotte Island compared to what we observed in the Distal swarm. This may support the interpretation of Feuillet et al. (2021) who deduced a N-S local extension from the orientation of Mayotte's western ridge and from various cones and other volcanic features.

Large caldera collapses resulting from significant intrusions are sometimes associated with eruptions along caldera structures. This has been observed, for example, at Fernandina (Galapagos) and Miyakejima (Japan) volcanoes (e.g. Howard, 2010; Nakada et al., 2005). When the piston collapses, magma can be transferred from the deepest reservoir towards the surface in the space created along its flanks. The caldera structure proposed here is confined in the mantle and we have evidence of two reservoirs above and below it (R1 at the base and R3 at the summit). It is therefore plausible that magma transferred between them when the piston collapsed (Fig. 7b).

Based on the volume of lava erupted (approx. 6.5 km^3, REVOSIMA, 2024), simple first-order assumptions can be made about the piston's fall and the volume of magma that could have travelled within the system. Given the geometry of the piston (4 km diameter at the top and 8 km at the base), a subsidence of ~80 m would imply a volume decrease of ~4 km^3 in reservoir R1 and a volume increase of ~ +1 km^3 in reservoir R3. A ~10 m wide space would have been created between the piston and the surrounding wall in which up to ~ 3 km^3 of magma could be retained. Such a scenario is incompatible with the eruption at Fani Maoré, because all the magma would have been kept within the caldera structure. This simple geometric model does not, however, take into account the relaxation of the ~3 km-thick seismically-active, conical wall surrounding the piston.

An elastic strain of 3×10^{-3} (at the limit of the elastic domain) distributed throughout the wall would reduce the space between the piston and the wall by ~9 m. This value is probably conservative as the material is not purely elastic, as demonstrated by the presence of brittle failure evidenced by the earthquakes. In this case, the volume of magma that could have been trapped in this 1m-wide space would be reduced to ~0.3 km^3, leaving a magma volume of 2.7 km^3 to fuel the distal eruption. This volume approximately matches the 2.5 km^3 dense-rock equivalent (DRE) volume estimated at Fani Maoré in May 2019 (Feuillet et al., 2021).

Given the cone's lateral surface area (~285 km^2) and considering a rigidity modulus varying between 3.3 GPa (for highly fractured domain) and 33 GPa (a more standard value), a fall of about 80 m, would generate a geodetic moment ranging from 7.5×10^{19} Nm to 7.5×10^{20} Nm. This corresponds to a magnitude Mw between ~7 and ~8. These ranges of moment values and magnitudes are far larger than those recorded during the seismic crisis in the Proximal swarm (Mercury et al., 2022; Saurel et al., 2022) suggesting that the piston fall is largely aseismic.

Between May 2019 and the end of September 2020, an additional 1.5 km^3 of lava erupted at Fani Maoré (REVOSIMA, 2024), (~1 km^3 DRE using the 27 % vesicularity estimated by Berthod et al., 2021a). According to our piston model, 1 km^3 of additional magma erupted would correspond to an additional piston fall of ~ 30 m with a geodetic Mo ranging from $2.8E^{+19}$ Nm to $2.8E^{+20}$ Nm (Mw=~7 to ~7.5). For the same period, Saurel et al., 2022 provided a complete seismic catalog from which we calculated a cumulative seismic moment for the Proximal swarm that reached $2E^{+17}$ Nm, corresponding to a Mw=5.5 earthquake. This value is about 100 to 1000 times less than the geodetic estimate above. The piston fall was thus mostly aseismic (99% to 99.9%) perhaps because the piston was lubricated by the magma rising along its edges towards R3. In any case, this is in agreement with the balance of seismic/aseismic strain estimated during the 65 m Bardarbunga piston collapse (at least 90% aseismic strain, Gudmundsson et al., 2016; Ágústsdóttir et al., 2019).

The mechanisms involved in the Mayotte eruption are similar to those observed during other large worldwide, basaltic, fissure eruptions: the drainage of a reservoir by a dyke and a subsequent caldera collapse. However, the delay between the onsets of the dyke intrusion and of the piston collapse appears to have been longer in the case of Mayotte: 1–2 months (Lemoine et al., 2020; Mercury et al., 2022) instead of ~few days at Bardarbunga for example. This could be explained by the fact that the piston is deeper in the mantle and that several reservoirs are involved. From the timing of the seismicity (Lemoine et al., 2020; Feuillet et al., 2021, Mercury et al. 2022), we know that the earthquakes started in the northwestern part of the Distal swarm, and then propagated eastward and upward to reach the seafloor below Fani Maoré. After that, seismic activity began at the Proximal swarm above R1, which was likely hydraulically connected to R2 and started to deflate in turn; as a result, the piston began to fall, coevally with a strong increase of the flow rate as estimated from modeling of land and seafloor surface deformations (Peltier et al., 2022). The piston fall likely sustained the exceptionally long eruption that ended in late 2020 (REVOSIMA, 2024). Our first order geometric calculation implies that the R3 reservoir above the piston was filled by about 1 km^3 of magma escaping from R1 and flowing upward along the caldera structure during the piston fall of about 100 m (Fig. 7b). This transfer of magma may cancel the pressure drop in R3 after each piston drop and maintain the R3 reservoir at a constant pressure. A piston fall combined with magma transfer between the two reservoirs may be the source of the exceptional long-lasting and monochromatic Very Low Frequency earthquakes (VLF), observed during this crisis (e.g. Cesca et al., 2020; Lemoine et al. 2020), and located at 22±15 km depth bsl above the center of the Proximal swarm (Fig. 7a, Laurent, 2023; Laurent et al., 2019; Feuillet et al., 2021).

The absence of seismicity above ~25 km suggests that magma storage is currently confined within the mantle. We have no evidence of motion along shallower caldera structures. Nevertheless, we cannot rule out aseismic (plastic) behavior within the crust, but we have still no evidence for caldera collapse, active faulting, or lava flows at the seafloor above the Proximal swarm since May 2018 (REVOSIMA, 2024, Puzenat et al., 2022). However, shallower caldera structures have been activated in the past, as attested by the existence of an ancient 8 km-wide caldera structure on the seafloor, located directly above the Proximal swarm, crowned by large lava flows, cones and eruptive fissures (Feuillet et al., 2021; Puzenat et al., 2022). It is worth noting that most of the volcanic products sampled from this area, as the phonolite lavas in Figs. 1, 2 and 4, are more evolved magmas that resulted from fractional crystallization of more mafic magma in the mantle (Berthod et al., 2021b). These phonolites may originate from R3 (Foix et al., 2021).

The arrival of a deep, hot, and CO_2-rich mafic magma (from R1) into the deeper parts of R3 may have led to its destabilization and pressurization, modifying the physical properties of magmas (density, viscosity, and buoyancy) and resulting in an upward accumulation of exsolved fluid (e.g. CO_2) within a short time scale (e.g., Folch and Marti, 1998; Klug et al., 2020). Such a process could explain the intensifying fluid

flow (causing acoustic plumes) documented in the Horse-Shoe area (Scalabrin, 2023; REVOSIMA, 2024) and detected by every oceanographic cruise since the eruption started (e.g. Rinnert et al., 2019). Depending on the degree of destabilization, the arrival of this new magma could potentially foster the upward propagation of deformation along the pre-existing caldera structure and/or trigger an eruption above R3.

The presence of a 45 km-high caldera-like structure in the lithosphere has not been documented elsewhere and one might argue that it is very difficult to maintain volcanic reservoirs at such depths. Numerical models however suggest that this structure may be the result of a long-lived interaction between the overlying reservoirs in a highly damaged medium (De Sagazan et al., 2024) that is expected for an old ocean lithosphere weakened by numerous fractures zones and altered by fluid circulation and/or thermal processes.

5. Conclusions

We used seismological data collected over nine months by a dense array of ocean-bottom seismometers (OBS's), starting in February 2019, deployed to enhance the monitoring of the eruption of Fani Maoré, the newborn volcano offshore Mayotte. The 2677 earthquakes we relocated show well-defined mantle structures in two separate earthquake swarms. This seismicity is organized, between 20 and 55 km bsl, in 10–15 km-high, 10–15 km-wide and 1–4 km-narrow structures. We calculated 300 focal mechanisms, allowing us to decipher the forces controlling these structures. These results outline a dyke in the Distal swarm and an outward-dipping ring-fault zone delineating a piston-like structure in the Proximal swarm. This is the first time that brittle deformations along such volcano-tectonic structures have been documented in the mantle from such well-located deep seismicity. While large faults had been imaged down to 45 km in the oceanic lithosphere in the Wharton Basin, using seismic reflection methods (Qin and Singh, 2015), our results highlight active seismogenic structures of comparable size crosscutting a large part of another oceanic lithosphere.

According to our results and in light of previous works, we interpret that, the two swarms are linked to one-another by a large magma withdrawal from a mantle reservoir (R1), causing collapse of the piston above, and feeding the eruption through the dyke. The piston-fall likely sustained the driving pressure to feed the largest ever-documented submarine eruption (~6.5 km^3 lava flows).

We propose the following piston model: around the piston, normal faulting occurs on an array of inward dipping patches. Strike-slip and normal faulting allow the elastic relaxation of the damage zone around the piston. This process is largely aseismic, which strongly suggests that the piston fall, likely about 100 m, is partly accommodated by magma flowing up around it to a smaller reservoir (R3) just above.

The absence of crustal earthquakes in our study is intriguing. There are probably at least three reasons for this: 1) below Fani Maoré, there are only very small magnitude, shallow earthquakes (if any) and the significant ones only occurred in June 2018, before a robust seismic network was in place and just before the dyke pierced the seafloor (e.g. Mercury et al., 2022), as is observed during the early phases of other basaltic eruptions (e.g. Einarsson, 2018); 2) above the Proximal earthquake swarm, the shallow, inferred ring-fault zone did not get activated; 3) if the crust is weak (serpentinized), the crustal part of the ring-fault zone may be already creeping.

This work answers some questions, but raises others. Did the piston slip continuously or intermittently and how might this have controlled the flux of magma to the seafloor? Is the magma circulating around the piston the cause of the LP earthquakes (e.g. Hensch et al., 2019; Soosalu et al., 2010) that were observed (Retailleau et al., 2022)? The meaning of the weak and diffuse seismicity in the western quarter of the proximal swarm remains unclear. This could be a sign that the western side of the piston is more lubricated/hotter, perhaps related to magma/fluids (e.g. CO2) leakages towards the volcanic plumbing system of Petite Terre. Note that an uneven distribution of seismicity was also observed around the piston that collapsed 65 m during the 2014–2015 Bárðarbunga eruption in Iceland (e.g. Gudmundsson et al., 2016; Ágústsdóttir et al., 2019).

This work highlights the value of deploying OBS's to decipher crustal and mantle processes behind intraplate eruptions that occur in many submarine regions and have the potential to affect human populations on nearby inhabited islands.

Data availability

Ship-borne bathymetric data from the MAYOBS1 cruise can be obtained through the French national oceanographic data center SISMER (http://en.data.ifremer.fr/SISMER, doi:10.17600/18,001,217).

In addition to the bathymetric data from the MAYOBS1 cruise, bathymetric data around Mayotte (from the Bathymay cruise, doi:10.17600/4,200,020), topographic data of Mayotte Island (Litto3D Mayotte, https://diffusion.shom.fr/presentation/ litto3d-mayot2012.html) and bathymetric compilation of the General Bathymetric Chart of the Oceans (https://www.gebco.net) were used.

Used land stations belong to the 7 following networks. RA: RESIF-RAP french accelerometric network (doi:10.15778/RESIF.RA): YTMZ and MILA stations. II: Global Seismic Network IRIS-IDA (doi:10.7914/SN/II): PMZI station. QM: Comoros archipelago seismic and volcanic network (doi:10.18715/MAYOTTE.QM.): KNKL, MTSB, and GGLO stations*. AM: Raspberry Shake network (doi:10.7914/SN/AM): R0CC5, R1EE2 and RAE55 stations, data are acquired by Raspberry Shake SA company and made available from IRIS data centre and Raspberry Shake SA data centre. ED: EduSismo network: MCHI station, data is available upon request at http://www.edusismo.org/. KA: Observatoire Volcanologique du Karthala,: CAB, DEMB, and SBC stations, data upon request at Centre National de Documentation et de Recherche Scientifique (cndrs@comorestelecom) or from Mr Hamidi Soulé (soulehamid@gmail.com), director of the Karthala Observatory . GE: GEOFON netword: SBV station (Madagasar): doi:10.14470/TR560404. Used OBS came from 2 pools of instruments of INSU-IPGP and IFREMER. The INSU-IPGP pool of OBS MOXX* is managed and operated by IPGP and CNRS (https://parc-obs.insu.cnrs.fr/). OBS MicrOBS IF##A-D* are operated by IFREMER/Ressources physiques et Ecosystèmes de fond de Mer/département de Géosciences Marines/service de Cartographie et Traitement de Données d'Instrumentation. Data from station or OBS marked with * are available upon request at IPGP data centre (http://datacenter.ipgp.fr).

Past felt earthquakes statistics on Mayotte from SisFrance database: http://www.sisfrance.net.

HypoDD v2.1 software (earthquake relative relocations, https://www.ldeo.columbia.edu/~felixw/hypoDD.html) can be obtained upon request from Mr F. Waldhauser (felixw@ldeo.columbia.edu).

FPFIT v1.5 software (focal mechanism inversions) can be obtained at https://www.usgs.gov/software/fpfit-fpplot-and-fppage.

The figures were produced using the open source softwares gfortran (https://gcc.gnu.org/wiki/Gfortran) and GMT (https://www.generic-mapping-tools.org/) and Adobe illustrator software (https://www.adobe.com/).

Funding

The Tellus SISMAYOTTE project (broad-band land stations and first OBSs, MAYOBS1, doi:10.17600/18001217) was funded by INSU, CNRS and the French Ministry of Environment (ministère de la transition écologique et solidaire—MTES).This study was carried out in the frame work of the ANR COYOTES (ANR-19-CE31-0018, https://anr.fr/Projet-ANR-19-CE31-0018) project funded by the French ANR (Agence Nationale de Recherche) and the BRGM (Pdev Mayotte) .Since June 2019, all activities on Mayotte are funded by le Ministère de

l'Enseignement Supérieur, de la Recherche et de l'Innovation (MESRI), le Ministère de la Transition Ecologique (MTE), le Ministère des Outremers (MOM), le Ministère de l'Intérieur (MI), and le Ministère des Armées with the support of the DIRMOM (Direction Interministérielle aux Risques Majeurs en Outremer). This project has also received funding from the Réseau de Surveillance Volcanologique et Sismologique de Mayotte (REVOSIMA), from the European Union's Horizon 2020 research and innovation program under grant agreement No 731,070 and for additional support under internal funds from the CNRS/INSU, IPGP, IFREMER, BRGM. All the OBS deployments and recoveries are performed as part of the MAYOBS set of cruises (doi:10.18142/291).

CRediT authorship contribution statement

E. Jacques: Conceptualization, Investigation, Software, Validation, Writing – review & editing, Writing – original draft. **R. Hoste-Colomer:** Writing – review & editing, Software, Methodology. **N. Feuillet:** Investigation, Writing – review & editing, Funding acquisition, Conceptualization. **A. Lemoine:** Writing – review & editing, Validation, Investigation, Funding acquisition. **J. van der Woerd:** Writing – review & editing, Conceptualization. **W.C. Crawford:** Writing – review & editing, Project administration. **C. Berthod:** Writing – review & editing, Conceptualization. **P. Bachèlery:** Writing – review & editing, Conceptualization.

Declaration of competing interest

The authors declare that they have no known competing financial interests or personal relationships that could have appeared to influence the work reported in this paper.

Data availability

I have share the link to my data/code in the section Data availability

Acknowledgement

We thank the REVOSIMA seismology group, BCSF/ReNaSS, and OVPF-IPGP for the picking of the data, discussion and support. This work benefited from seismic data shared by the Karthala volcanologic observatory (OVK).

We thank Aude Lavayssière for sharing the catalog of the 2680 best located earthquakes we used (Lavayssière et al., 2022). The MCHI station (Sismo à l'Ecole, http://edumed.unice.fr/fr) was installed by Didier Bertil and Alison Colombain, with funding from BRGM, DEAL-Mayotte and Rectorat de Mayotte.The RaspBerry Shake instruments were installed by Maxime Bès de Berc, Marc Grunberg, Christophe Sira and Antoine Schlupp.The Mayotte stations were installed by Maxime Bès de Berc, Jérôme van der Woerd, Céleste Broucke, Alison Colombain, Hélène Jund and Grégoire Dectot. The Grande Glorieuse station was installed by Aline Peltier and Philippe Kowalski. They are maintained by CNRS/EOST/IPGS, BRGM and OVPF-IPGP through the REVOSIMA. OBS are deployed, recovered, maintained and data pre-processed by Romuald Daniel, Simon Besançon, Wayne Crawford and Jérémy Gomez. MicrOBS are deployed, recovered, maintained and data pre-processed by Pascal Pelleau, Pierre Guyavarch and Mickaël Roudault.

We thank the captains and crews of the R/V Marion Dufresne, R/V Pourquoi Pas?. R/V Champlain and LCT Ylang. Mayotte land-stations are maintained by CNRS/EOST/IPGS, BRGM and OVPF-IPGP and the OBS are recovered, maintained and data pre-processed by CNRS/INSU and IFREMER.

We thank the IPGP for general funding to the Observatoires Volcanologiques et Sismologiques (OVS). The data contributes to the Service National d'Observation en Volcanologie (SNOV).

We are also grateful for the constructive reviews provided by Páll Einarsson and William Chadwick, and editorial handling by Chiara Petrone.

Supplementary materials

Supplementary material associated with this article can be found, in the online version, at doi:10.1016/j.epsl.2024.119026.

References

Acocella, V., 2007. Understanding caldera structure and development: an overview of analogue models compared to natural calderas. Earth-Sci. Rev. 85 (3–4), 125–160. https://doi.org/10.1016/j.earscirev.2007.08.004.

Ágústsdóttir, T., Woods, J., Greenfield, T., Green, R.G., White, R.S., Winder, T., Brandsdóttir, B., Steinthórsson, S., Soosalu, H, 2016. Strike-slip faulting during the 2014 Bárðarbunga-Holuhraun dike intrusion, central Iceland. Geophys. Res. Lett. 43 (4), 1495–1503. https://doi.org/10.1002/2015GL067423.

Ágústsdóttir, T., Winder, T., Woods, J., White, R.S., Greenfield, T., Brandsdóttir, B., 2019. Intense seismicity during the 2014–2015 Bárðarbunga-Holuhraun rifting event, Iceland, reveals the nature of dike-induced earthquakes and caldera collapse mechanisms. J. Geophys. Res.: Solid Earth 124 (8), 8331–8357. https://doi.org/10.1029/2018JB016010.

D'Auria, L., Koulakov, I., Prudencio, J., Cabrera-Pérez, I., Ibáñez, J.M., Barrancos, J., García-Hernández, R., Martínez van Dorth, D., Padilla, G.D., Przeor, M., Ortega, V., Hernández, P., Peréz, N.M, 2022. Rapid magma ascent beneath La Palma revealed by seismic tomography. Sci. Rep. 12 (1), 17654. https://doi.org/10.1038/s41598-022-21818-9.

Berthod, C., Médard, E., Bachèlery, P., Gurioli, L., Di Muro, A., Peltier, A., Komorowski, J., Benbakkar, M., Devidal, J., Langlade, J., Besson, P., Boudon, G., Rose-Koga, E., Deplus, C., Le Friant, A., Bickert, M., Nowak, S., Thinon, I., Burckel, P., Hidalgo, S., Jorry, S., Fouquet, Y., Feuillet, N, 2021a. The 2018-ongoing Mayotte submarine eruption: magma migration imaged by petrological monitoring. Earth Planet. Sci. Lett. 571, 117085. https://doi.org/10.1016/j.epsl.2021.117085.

Berthod, C., Médard, E., Di Muro, A., Hassen Ali, T., Gurioli, L., Chauvel, C., Komorowski, J., Bachèlery, P., Peltier, A., Benbakkar, M., Devidal, J.L., Besson, P., Le Friant, A., Deplus, C., Nowak, S., Thinon, I., Burckel, P., Hidalgo, S., Feuillet, N., Jorry, S., Fouquet, Y., 2021b. Mantle xenolith-bearing phonolites and basanites feed the active volcanic ridge of Mayotte (Comoros archipelago, SW Indian Ocean). Contributions Mineral. Petrol. 176, 1–24. https://doi.org/10.1007/s00410-021-01833-1.

Berthod, C., Komorowski, J.C., Gurioli, L., Médard, E., Bachèlery, P., Besson, P., Verdurme, P., Chevrel, O., Di Muro, A., Peltier, A., Devidal, J.L., Nowak, S., Thinon, I., Burckel, P., Hidalgo, S., Deplus, C., Loubrieu, B., Pierre, D., Bermell, S., Pitel-Roudaut, M., Réaud, Y., Fouchard, S., Bickert, M., Le Friant, A., Paquet, F., Feuillet, N., Jorry, S., Fouquet, Y., Rinnert, E., Cathalot, C., Lebas, E., 2022. Temporal magmatic evolution of the Fani Maoré submarine eruption 50 km east of Mayotte revealed by *in situ* sampling and petrological monitoring. Comptes Rendus. Géoscience 354 (S2), 1–29. https://doi.org/10.5802/crgeos.155.

Bertil, D., Mercury, N., Doubre, C., Lemoine, A., Van der Woerd, J., 2021. The unexpected Mayotte 2018–2020 seismic sequence: a reappraisal of the regional seismicity of the Comoros. Comptes Rendus. Géoscience 353 (S1), 1–25. https://doi.org/10.5802/crgeos.79.

Baillard, C., Wilcock, W.S.D., Arnulf, A.F., Tolstoy, M., Waldhauser, F., 2019. A joint inversion for three-dimensional P and S wave velocity structure and earthquake locations beneath axial seamount. J. Geophys. Res.: Solid Earth 124. https://doi.org/10.1029/2019JB017970, 12,997–13,020.

Blanchette, A.R., Klemperer, S.L., Mooney, W.D., Zahran, H.M., 2018. Two-stage Red Sea rifting inferred from mantle earthquakes in Neoproterozoic lithosphere. Earth Planet. Sci. Lett. 497, 92–101. https://doi.org/10.1016/j.epsl.2018.05.048.

Bonny, E., Thordarson, T., Wright, R., Höskuldsson, A., Jónsdóttir, I., 2018. The volume of lava erupted during the 2014 to 2015 eruption at Holuhraun, Iceland: a comparison between satellite- and ground-based measurements. J. Geophys. Res.: Solid Earth 123, 5412–5426. https://doi.org/10.1029/2017JB015008.

Cesca, S., Letort, J., Razafindrakoto, H.N., Heimann, S., Rivalta, E., Isken, M.P., Nikkhoo, M., Passarelli, L., Petersen, G.M., Cotton, Dahm, T, 2020. Drainage of a deep magma reservoir near Mayotte inferred from seismicity and deformation. Nat. Geosci. 13 (1), 87–93. https://doi.org/10.1038/s41561-019-0505-5.

Craig, T.J., Copley, A., Jackson, J., 2014. A reassessment of outer-rise seismicity and its implications for the mechanics of oceanic lithosphere. Geophys. J. Int. 197 (1), 63–89. https://doi.org/10.1093/gji/ggu013.

Déverchère, J., Petit, C., Gileva, N., Radziminovitch, N., Melnikova, V., San'Kov, V., 2001. Depth distribution of earthquakes in the Baikal rift system and its implications for the rheology of the lithosphere. Geophys. J. Int. 146 (3), 714–730. https://doi.org/10.1046/j.0956-540x.2001.1484.484.x.

Einarsson, P., 2018. Short-term seismic precursors to Icelandic eruptions 1973–2014. Front. Earth Sci. 6, 45.

Famin, V., Michon, L., Bourhane, A., 2020. The Comoros archipelago: a right-lateral transform boundary between the Somalia and Lwandle plates. Tectonophysics 789, 228539. https://doi.org/10.3389/feart.2018.00045, 10.1016/j.tecto.2020.228539.

Feuillet, N., 2019. MAYOBS1 cruise. RV Marion Dufresne. https://doi.org/10.17600/18001217.

Feuillet, N., Jorry, S., Crawford, W., Deplus, C., Thinon, I., Jacques, E., Saurel, J..M., Lemoine, A., Paquet, F., Satriano, C., Aiken, C., Foix, O., Kowalski, P., Laurent, A.,

Rinnert, E., Cathalot, C., Donval, J..P., Guyader, V., Gaillot, A., Moreira, M., Peltier, A., Beauducel, F., Grandin, R., Ballu, V., Daniel, R., Pelleau, P., Besancon, S., Geli, L., Bernard, P., Bachelery, P., Fouquet, Y., Bertil, D., Lemarchand, A., Van der Woerd, J., 2021. Birth of a large volcanic edifice through lithosphere-scale dyking offshore Mayotte (Indian Ocean). Nat. Geosci. 14 (10), 787–795. https://doi.org/10.1038/s41561-021-00809-x.

Foix, O., Aiken, C., Saurel, J.M., Feuillet, N., Jorry, S.J., Rinnert, E., Thinon, I., 2021. Offshore Mayotte volcanic plumbing revealed by local passive tomography. J. Volcanol. Geothermal Res. 420, 107395. https://doi.org/10.1016/j.jvolgeores.2021.107395.

Folch, A., Martı, J., 1998. The generation of overpressure in felsic magma chambers by replenishment. Earth Planet. Sci. Lett. 163 (1–4), 301–314. https://doi.org/10.1016/S0012-821X(98)00196-4.

Gamond, J.F., 1983. Displacement features associated with fault zones: a comparison between observed examples and experimental models. J. Struct. Geol. 5, 33–45.

Grevemeyer, I., Hayman, N.W., Lange, D., Peirce, C., Papenberg, C., Van Avendonk, H.J., Florian Schmid, F., Gómez de La Peña, L., Dannowski, A, 2019. Constraining the maximum depth of brittle deformation at slow-and ultraslow-spreading ridges using microseismicity. Geology 47 (11), 1069–1073. https://doi.org/10.1130/G46577.1.

Gudmundsson, M.T., Jónsdóttir, K., Hooper, A., Holohan, E.P., Halldórsson, S.A., Ófeigsson, B.G., Cesca, S., Vogfjörd, K.S., Sigmundsson, F., Högnadóttir, T., Pálsson, F., Walter, T., Schöpfer, M., Heimann, S., Reynolds, H., Dumont, S., Bali, E., Gudfinnsson, G., Dahm, T., Roberts, M., Hensch, M., Belart, J., Spaans, K., Jakobsson, S., Gudmundsson, G., Fridriksdóttir, H., Drouin, V., Dürig, T., Aðalgeirsdóttir, G., Riishuus, M., Pedersen, G., van Boeckel, T., Oddsson, B., Pfeffer, M., Barsotti, S., Bergsson, B., Donovan, A., Burton, M., Aiuppa, A., 2016. Gradual caldera collapse at Bárdarbunga volcano, Iceland, regulated by lateral magma outflow. Science 353 (6296). https://doi.org/10.1029/2018JB016010.

Hensch, M., Dahm, T., Ritter, J., Heimann, S., Schmidt, B., Stange, S., Lehmann, K., 2019. Deep low-frequency earthquakes reveal ongoing magmatic recharge beneath Laacher See Volcano (Eifel, Germany). Geophys. J. Int. 216 (3), 2025–2036. https://doi.org/10.1093/gji/ggy532.

Howard, K.A., 2010. Caldera collapse: perspectives from comparing Galápagos volcanoes, nuclear-test sinks, sandbox models, and volcanoes on Mars. GSA Today 20 (10), 4–10. https://doi.org/10.1130/GSATG82A.1.

Inbal, A., Ampuero, J.P., Clayton, R.W., 2016. Localized seismic deformation in the upper mantle revealed by dense seismic arrays. Science 354 (6308), 88–92. https://doi.org/10.1126/science.aaf1370.

Jones, R.H., Stewart, R.C., 1997. A method for determining significant structures in a cloud of earthquakes. J. Geophys. Res.: Solid Earth 102 (B4), 8245–8254. https://doi.org/10.1029/96JB03739.

Klug, J.D., Singer, B.S., Kita, N.T., Spicuzza, M.J., 2020. Storage and evolution of Laguna Del Maule rhyolites: insight from volatile and trace element contents in melt inclusions. J. Geophys. Res.: Solid Earth 125 (8), e2020JB019475. https://doi.org/10.1029/2020JB019475.

Kuna, V.M., Nábělek, J.L., Braunmiller, J., 2019. Mode of slip and crust–mantle interaction at oceanic transform faults. Nat. Geosci. 12 (2), 138–142. https://doi.org/10.1038/s41561-018-0287-1.

Kissling, E., Kradolfer, U., Maurer, H., 1995. Program VELEST User's Guide-Short Introduction. Institute of Geophysics, ETH Zurich.

Laurent, A., Satriano, C., & Bernard, P. (2019, November). Detection, location and characterization of VLF events during the 2018-2019 seismovolcanic crisis in Mayotte. In Rencontres scientifiques et techniques RESIF 2019. https://hal.archives-ouvertes.fr/hal-02446050.

Lavayssière, A., Drooff, C., Ebinger, C., Gallacher, R., Illsley-Kemp, F., Oliva, S.J., Keir, D., 2019. Depth extent and kinematics of faulting in the southern Tanganyika rift. Afr. Tectonics 38, 842–862. https://doi.org/10.1029/2018TC005379, 10.1029/2018TC005379.

Laurent, A., 2023. Détection, localisation et caractérisation des évènements Very Low Frequency (VLF) de la crise sismo-volcanique de Mayotte (2018-2022). PhD. thesis. Université Paris Cité, France.

Lavayssière, A., Bazin, S., Royer, J.Y., 2024. Hydroacoustic monitoring of Mayotte submarine volcano during Its eruptive phase. Geosciences 14 (6), 170. https://doi.org/10.3390/geosciences14060170.

Lavayssière, A., Crawford, W.C., Saurel, J.M., Satriano, C., Feuillet, N., Jacques, E., Komorowski, J.C., 2022. A new 1D velocity model and absolute locations image the Mayotte seismo-volcanic region. J. Volcanol. Geothermal Res. 421, 107440. https://doi.org/10.1016/j.jvolgeores.2021.107440.

Lee, W.H.K., Lahr, J.C., 1972. HYPO71: a Computer Program for Determining hypocenter, magnitude, and First Motion Pattern of Local earthquakes. (No. 72-224). US Dept. of the Interior, Geological Survey. National Center for Earthquake Research. https://doi.org/10.3133/ofr72224.

Lemoine, A., Briole, P., Bertil, D., Roullé, A., Foumelis, M., Thinon, I., Raucoules, D., de Michele, M., Valty, P., Hoste Colomer, R., 2020. The 2018–2019 seismo-volcanic crisis east of Mayotte, Comoros islands: seismicity and ground deformation markers of an exceptional submarine eruption. Geophys. J. Int. 223 (1), 22–44. https://doi.org/10.1093/gji/ggaa273.

Lomax, A., Michelini, A., Curtis, A., 2014. Earthquake location, direct, global-search methods. Encyclopedia of Complexity and System Science, 2nd ed. Springer, New York, pp. 1–33. https://doi.org/10.1007/978-3-642-27737-5_150-2.

Martí, J., Pinel, V., López, C., Geyer, A., Abella, R., Tárraga, M., Blanco, M.J., Rodríguez, C, 2013. Causes and mechanisms of the 2011–2012 El Hierro (Canary Islands) submarine eruption. J. Geophys. Res.: Solid Earth 118 (3), 823–839. https://doi.org/10.1002/jgrb.50087.

Masquelet, C., Watremez, L., Leroy, S., Sauter, D., Delescluse, M., Chamot-Rooke, N., Ringenbach, J.C., Thinon, I., Lemoine, A., Franke, D., 2024. Intra-oceanic emplacement of the Comoros Archipelago through inherited fracture zones, in press. Tectonophysics. https://doi.org/10.1016/j.tecto.2024.230348.

Mittal, T., Jordan, J.S., Retailleau, L., Beauducel, F., Peltier, A., 2022. Mayotte 2018 eruption likely sourced from a magmatic mush. Earth Planet. Sci. Lett. 590, 117566. https://doi.org/10.1016/j.epsl.2022.117566.

Mercury, N., Lemoine, A., Doubre, C., Bertil, D., van Der Woerd, J., Hoste-Colomer, R., Battaglia, J., 2022. Onset of a submarine eruption east of Mayotte, Comoros archipelago: the first ten months seismicity of the seismo-volcanic sequence (2018–2019). Comptes Rendus. Géosci. 354 (S2), 105–136. https://doi.org/10.5802/crgeos.191.

Monsalve, G., Sheehan, A., Schulte-Pelkum, V., Rajaure, S., Pandey, M.R., Wu, F., 2006. Seismicity and one-dimensional velocity structure of the Himalayan collision zone: earthquakes in the crust and upper mantle. J. Geophys. Res. 111, B10301. https://doi.org/10.1029/2005JB004062.

Mori, J., White, R.A., Harlow, D.H., Okubo, P., Power, J.A., Hoblitt, R.P., Newhall, C.G., 1996. Volcanic Earthquakes Following the 1991 Climactic Eruption of Mount Pinatubo: Strong seismicity During a Waning Eruption. Fire and Mud: Eruptions and Lahars of Mount Pinatubo, Philippines, pp. 339–350.

Nakada, S., Nagai, M., Kaneko, T., Nozawa, A., & Suzuki-Kamata, K. (2005). Chronology and products of the 2000 eruption of Miyakejima Volcano, Japan. Bull. Volcanol., 67, 205–218. https://doi.org/10.1007/s00445-004-0404-4.

Neal, C.A., Brantley, S.R., Antolik, L., Babb, J.L., Burgess, M., Calles, K., … & Damby, D. (2019). The 2018 rift eruption and summit collapse of Kīlauea Volcano. Science, 363 (6425), 367–374.

Nicolas, A., 1984. Principes De Tectonique. Masson, Paris, p. 196.

Paige, C.C., Saunders, M.A., 1982. LSQR: sparse linear equations and least squares problems. ACM Trans. Math. Softw. 8/2, 195–209. https://doi.org/10.1145/355993.356000.

Peltier, A., Saur, S., Ballu, V., Beauducel, F., Briole, P., Chanard, K., Daussed, D., De Chabalier, J.B., Grandin, G., Rouffiac, P., Tranchant, Y.T., Bès de Berc, M., Besançon, S., Boissier, P., Broucke, C., Brunet, C., Canjamalé, K., Carme, E., Catherine, P., Colombain, A., Crawford, W., Daniel, R., Dectot, G., Desfete, N., Doubre, C., Dumouch, T., Griot, C., Grunberg, M., Jund, H., Philippe Kowalski, P., Lauret, F., Lebreton, J., Pesqueira, F., Tronel, F., Valty, P., Van Der Woerd, J, 2022. Ground deformation monitoring of the eruption offshore Mayotte. Comptes Rendus. Géosci. 354 (S2), 1–23. https://doi.org/10.5802/crgeos.176.

Puzenat, V., Feuillet, N., Komorowski, J.C., Escartín, J., Deplus, C., Bachèlery, P., Berthod, C., Gurioli, L., Scalabrin, C., Cécile Cathalot, C., Rinnert, E., Loubrieu, B., Pierre, D., Pitel-Roudaut, M., Tanguy, N., Fouquet, Y., Jorry, J.S., Lebas, E., Paquet, F., Thinon, I., 2022. Volcano-tectonic structures of Mayotte's upper submarine slope: insights from high-resolution bathymetry and in-situ imagery from a deep-towed camera. Comptes Rendus. Géosci. 354 (S2), 81–104. https://doi.org/10.5802/crgeos.175.

Qin, Y., Singh, S.C., 2015. Seismic evidence of a two-layer lithospheric deformation in the Indian Ocean. Nat. Commun. 6 (1), 8298. https://doi.org/10.1038/ncomms9298.

Reasenberg, P.A., Oppenheimer, D., Lahr, J.C., Stephens, C.D., Page, R.A., 1986. Alaska Project version of FPFIT, FPPLOT and FPPAGE: fortrancomputer programs for calculating and displaying earthquake fault-plane solutions. U. S. Geol. Surv. Open File Rep. 86, 37.

Roche, O., Druitt, T.H., Merle, O., 2000. Experimental study of caldera formation. J. Geophys. Res.: Solid Earth 105 (B1), 395–416. https://doi.org/10.1029/1999JB900298.

Rodríguez-Cardozo, F., Hjörleifsdóttir, V., Jónsdóttir, K., Iglesias, A., Franco, S.I., Geirsson, H., Trujillo-Castrillón, N., Hensch, M., 2021. The 2014–2015 complex collapse of the Bárðarbunga caldera, Iceland, revealed by seismic moment tensors. J. Volcanol. Geothermal Res. 416, 107275. https://doi.org/10.1016/j.jvolgeores.2021.107275.

Retailleau, L., Saurel, J.M., Laporte, M., Lavayssière, A., Ferrazzini, V., Zhu, W., Beroza, G., Satriano, C., Komorowski, J., Team, O.V.P.F., 2022. Automatic detection for a comprehensive view of Mayotte seismicity. Comptes Rendus. Géoscience 354 (S2), 153–170. https://doi.org/10.5802/crgeos.133.

REVOSIMA (2024), Bulletin mensuel de l'activité sismo-volcanique à Mayotte, du 1 au 31 mars 2024. ISSN : 2680-1205. https://www.ipgp.fr/wp-content/uploads/2024/04/Revosima_bull_20240408.pdf.

Rinnert, E., Feuillet, N., Fouquet, Y., Jorry, S., Thinon, I., & Lebas, E. (2019). MAYOBS cruises, https://doi.org/10.18142/291.

de Sagazan, C., Retailleau, L., Gerbault, M., Peltier, A., Feuillet, N., Fontaine, F.J., Crawford, W.C., 2024. Seismicity near Mayotte explained by interacting magma bodies: insights from numerical modeling. J. Volcanol. Geothermal Res. 446, 107985. https://doi.org/10.1016/j.jvolgeores.2023.107985.

Scalabrin, C. (2023). Site d'émissions de fluides, Mayotte, zone Fer à Cheval (C. Scalabrin, 2022). Ifremer GEO-OCEAN. https://doi.org/10.12770/070818f6-6520-49e4-bafd-9d4d0609bf7d.

Sigmundsson, F., 2019. Calderas collapse as magma flows into rifts. Science 366 (6470), 1200–1201. https://doi.org/10.1126/science.aaz7126.

Singh, S.C., Hananto, N., Qin, Y., Leclerc, F., Avianto, P., Tapponnier, P.E., Carton, H., Wei, S., Nugroho, A.B., Gemilang, W.A., Sieh, K., Barbot, S., 2017. The discovery of a conjugate system of faults in the Wharton Basin intraplate deformation zone. Sci. Adv. 3 (1), e1601689. https://doi.org/10.1126/sciadv.1601689.

Saurel, J.M., Jacques, E., Aiken, C., Lemoine, A., Retailleau, L., Lavayssière, A., Foix, O., Dofal, A., Laurent, A., Mercury, N., Crawford, W., Lemarchand, A., Daniel, R., Pelleau, P., Bès de Berc, M., Dectot, G., Bertil, D., Roullé, A., Broucke, C., Colombain, A., Jund, H., Besançon, S., Guyavarch, P., Kowalski, P., Roudaut, M., Apprioual, R., Battaglia, J., Bodihar, S., Boissier, P., Bouin, M.P., Brunet, C., Canjamale, K., Catherine, P., Desfete, N., Doubre, C., Dretzen, R., Dumouche, T.,

Fernagu, P., Ferrazzini, V., Fontaine, F.R., Gaillot, A., Géli, L., Griot, C., Grunberg, M., Can Guzel, E., Hoste-Colomer, R., Lambotte, S., Lauret, F., Léger, F., Maros, E., Peltier, A., Vergne, J., Satriano, C., Tronel, F., Van der Woerd, J., Fouquet, Y., Jorry, S.J., Rinnert, E., Feuillet, N., 2022. Mayotte seismic crisis: building knowledge in near real-time by combining land and ocean-bottom seismometers, first results. Geophys. J. Int. 228 (2), 1281–1293. https://doi.org/10.1093/gji/ggab392.

Shreve, T., Grandin, R., Boichu, M., Garaebiti, E., Moussallam, Y., Ballu, V., Delgado, F., Leclerc, F., Vallée, M., Henriot, N., Cevuard, S., Tari, D., Lebellegard, P., Pelletier, B., 2019. From prodigious volcanic degassing to caldera subsidence and quiescence at Ambrym (Vanuatu): the influence of regional tectonics. Sci. Rep. 9 (1), 1–13. https://doi.org/10.1038/s41598-019-55141-7.

Soosalu, H., Key, J., White, R.S., Knox, C., Einarsson, P., Jakobsdóttir, S.S., 2010. Lower-crustal earthquakes caused by magma movement beneath Askja volcano on the north Iceland rift. Bull. Volcanol. 72, 55–62. https://doi.org/10.1007/s00445-009-0297-3.

Staudacher, T., Ferrazzini, V., Peltier, A., Kowalski, P., Boissier, P., Catherine, P., Lauret, F., Massin, F., 2009. The April 2007 eruption and the Dolomieu crater collapse, two major events at Piton de la Fournaise (La Réunion Island, Indian Ocean). J. Volcanol. Geothermal Res. 184 (1–2), 126–137. https://doi.org/10.1016/j.jvolgeores.2008.11.005.

Tkalčić, H., Dreger, D.S., Foulger, G.R., Julian, B.R., 2009. The puzzle of the 1996 Bárdarbunga, Iceland, earthquake: no volumetric component in the source mechanism. Bullet. Seismol. Soc. Am. 99 (5), 3077–3085. https://doi.org/10.1785/0120080361.

Thinon, I., Lemoine, A., Leroy, S., Paquet, F., Berthod, C., Zaragosi, S., Famin, V., Feuillet, N., Boymond, P., Masquelet, C., Mercury, N., Rusquet, A., Scalabrin, C., Van der Woerd, J., Bernard, J., Bignon, J., Clouard, V., Doubre, C., Jacques, E., Jorry, S., Rolandone, F., Chamot-Rooke, N., Delescluse, M., Franke, D., Watremez, L., Bachèlery, P., Michon, L., Sauter, D., Bujan, S., Canva, A., Dassie, E., Roche, V., Ali, S., Sitti Allaouia, A.H., Deplus, C., Rad, S., Sadeski, L., 2022. Volcanism and tectonics unveiled in the Comoros Archipelago between Africa and Madagascar. Comptes Rendus. Géoscience 354 (S2), 7–34. https://doi.org/10.5802/crgeos.159.

Toda, S., Stein, R.S., Sagiya, T., 2002. Evidence from the AD 2000 Izu islands earthquake swarm that stressing rate governs seismicity. Nature 419 (6902), 58–61. https://doi.org/10.1038/nature00997.

Torres-González, P.A., Luengo-Oroz, N., Lamolda, H., D'Alessandro, W., Albert, H., Iribarren, I., Moure-García, D., Soler, V., 2020. Unrest signals after 46 years of quiescence at cumbre vieja, La Palma, Canary Islands. J. Volcanol. Geothermal Res. 392, 106757. https://doi.org/10.1016/j.jvolgeores.2019.106757.

Vialon, P., 1979. Les déformations continues-discontinues des roches anisotropes. Eclogae Geol. Helv. 72, 531–549.

Waldhauser, F., 2001. hypoDD: a program to compute double-difference hypocenter locations (hypoDD version 1.0, 03/2001). U. S. Geol. Surv.Open File Rep. 01–113.